

## RESEARCH ARTICLE

# Structure–property relations of silicon oxycarbides studied using a machine learning interatomic potential

Niklas Leimeroth  | Jochen Rohrer  | Karsten Albe 

Institut für Materialwissenschaft,  
Technische Universität Darmstadt,  
Darmstadt, Germany

**Correspondence**

Niklas Leimeroth, Institut für  
Materialwissenschaft, Technische  
Universität Darmstadt, Otto-Berndt-Str. 3,  
64287 Darmstadt, Germany.  
Email: [leimeroth@mm.tu-darmstadt.de](mailto:leimeroth@mm.tu-darmstadt.de)

**Editor's Choice**

The Editor-in-Chief recommends this  
outstanding article.

**Funding information**

H2020 Societal Challenges, Grant/Award  
Number: 963542; Deutsche  
Forschungsgemeinschaft, Grant/Award  
Numbers: 405621137, 413956820;  
Bundesministerium für Bildung und  
Forschung, Grant/Award Number:  
03XP0390A

**Abstract**

Silicon oxycarbides show outstanding versatility due to their highly tunable composition and microstructure. Consequently, a key challenge is a thorough knowledge of structure–property relations in the system. In this work, we fit an atomic cluster expansion potential to a set of actively learned density-functional theory training data spanning a wide configurational space. We demonstrate the ability of the potential to produce realistic amorphous structures and rationalize the formation of different morphologies of the turbostratic free carbon phase. Finally, we relate the materials stiffness to its composition and microstructure, finding a delicate dependence on Si-C bonds that contradicts commonly assumed relations to the free carbon phase.

**KEYWORDS**

atomistic simulation, silicon oxycarbide, structure, Young's modulus

## 1 | INTRODUCTION

Silicon oxycarbides (Si-O-Cs) are highly versatile materials that combine remarkable structural and functional properties. Among them are high-temperature resistance, good mechanical strength,<sup>1,2</sup> great creep- and corrosion-resistance,<sup>3,4</sup> as well as piezoresistivity and the ability to reversibly store Li<sup>+</sup>, Na<sup>+</sup>, and K<sup>+</sup>.<sup>5–8</sup> These properties make them interesting for applications in very different fields, such as protective coatings,<sup>9</sup> energy storage,<sup>10</sup> and biomedicine.<sup>11</sup>

Despite the plethora of desirable properties and intensive research, open questions about structural features and their relation even to basic characteristics such as the Young's modulus (E) remain. From NMR measurements, it is known that Si-O-Cs consist of corner-shared SiO<sub>x</sub>C<sub>4–x</sub> tetrahedra with carbidic sp<sup>3</sup>-hybridized carbon<sup>12,13</sup> and

a segregated secondary phase with sp<sup>2</sup>-hybridized turbostratic carbon.<sup>14,15</sup> The detailed nanostructure, however, remains elusive and sensitively depends on the composition, precursor structure, and processing conditions. For example, it is still unclear in which form the turbostratic carbon is present in Si-O-C. Scarmi et al.<sup>16</sup> and Saha et al.<sup>17</sup> argued that interpenetrating networks of graphene-like carbon and silica-rich mixed tetrahedra domains are formed, based on the high creep resistance of the material. In contrast, Widgeon et al.<sup>12</sup> found that a model with graphitic inclusions embedded in a silica-rich matrix result in a better match of the mass fractal dimensions of mixed tetrahedra.

Here, atomistic simulations may help in understanding structure formation and structure–property relations of Si-O-C compounds at the nanoscale. As shown, for example, in a series of studies by Kroll,<sup>18–20</sup> ab-initio molecular

This is an open access article under the terms of the [Creative Commons Attribution](https://creativecommons.org/licenses/by/4.0/) License, which permits use, distribution and reproduction in any medium, provided the original work is properly cited.

© 2024 The Author(s). *Journal of the American Ceramic Society* published by Wiley Periodicals LLC on behalf of American Ceramic Society.

**TABLE 1** Compositions of hydrogen stripped polymers, sorted from low to high carbon content. These compositions were used to generate polymer derived (PD), bulk fragment (BF), isolated atoms (Ats), and graphite flakes and isolated atoms (GrAts) samples (see Figure 1A).

	$X_{\text{Si}}$	$X_{\text{O}}$	$X_{\text{C}}$
$\text{Si}_2\text{O}_2\text{C}$	0.4	0.4	0.2
PMSQ	0.25	0.5	0.25
RD-212	0.25	0.25	0.5
SILRES-604	0.125	0.125	0.75
RD-684	$\approx 0.121$	$\approx 0.121$	$\approx 0.758$

dynamics (MD) simulations can be employed to investigate structural details, energetics, and elastic properties of Si-O-C, but are limited to structures consisting of a few hundred or thousand atoms and simulation times on the order of tens of picoseconds. This makes nanoscale heterogeneities hard to capture and requires a careful preparation of model structures. Direct large-scale MD simulations, on the other hand, require suitable interatomic potentials and the complex nature of the strongly directional covalent bonds is hard to capture in empirical formulas like bond order potentials. Recent studies showed that the ReaxFF framework<sup>21</sup> allows investigating specific aspects of the Si-O-C system. For example, Newsome et al. simulated the oxidation of silicon carbide,<sup>22</sup> Soria et al.<sup>23,24</sup> investigated organic molecules on silicon surfaces, and Gao et al.<sup>25</sup> used the Newsome reaxFF to simulate the pyrolysis of specific polymers to amorphous Si-O-C. However, Ponomarev et al.<sup>26</sup> have shown that this parametrization, and the one by Soria et al. rupture mixed  $\text{SiO}_x\text{C}_{4-x}$  tetrahedra, which are essential parts of Si-O-C glass ceramics. In their work, they fitted a parameter set stabilizing these tetrahedra and also employed it to simulate pyrolysis processes. Of the three Si/O/C parameter sets, only the one by Newsome et al. is publicly available though.

Modern machine learning interatomic potentials (MLIPs) offer an alternative approach to describe complex systems, which does not rely on specific functional forms based on chemical insights. They can achieve high accuracies over a wide compositional and structural range at similar computational cost, but at the expense of requiring more training data. Recent studies have shown the successful application of MLIPs to carbon,<sup>27–34</sup> silicon,<sup>35–40</sup>  $\text{SiO}_2$ ,<sup>41–44</sup> and SiC.<sup>45,46</sup> In this work, we present an atomic cluster expansion (ACE) potential<sup>47</sup> for the Si-O-C system fitted to an extensive database generated using the active learning (AL) capabilities of moment tensor potential (MTPs)<sup>48</sup> and ACE.<sup>49</sup> We show that the potential achieves a high accuracy for a wide compositional range and that it can be used to produce realistic amorphous Si-O-C structures. We investigate structural features, formation

energies, and Young's moduli for samples with varying compositions and precursor configurations. Thereby, we find that the structure model containing graphene-like sheets and the graphitic inclusions in a silica matrix are both likely to describe the structure of Si-O-C, but occur at different stages of processing. Furthermore, we establish relations of Young's modulus to the fraction of Si-C bonds in mixed  $\text{SiO}_x\text{C}_{4-x}$  tetrahedra and the silica volume.

## 2 | METHODS

### 2.1 | Training and testing data

The training data for the potential were produced as follows. Initial Si, O, and Si-O structures were taken from an ACE potential previously fitted for the Si-O system.<sup>50</sup> Pure C structures were generated using the ASE package<sup>51</sup> with diamond, graphite, graphene, FCC, BCC, SC, and HCP lattices. SiC structures were taken from the materials project database.<sup>52</sup> Further C and SiC structure were created by applying random displacements and cell deformations.

Si-O-C structures with varying compositions were generated with two different procedures. First, structures were produced to match the expected coordination, that is, fourfold for Si and C and twofold for O.<sup>53,54</sup> Second, an AL procedure, schematically shown in Figure 1, was employed. Ternary systems based on the polymer derived (PD), bulk fragment (BF), and isolated atoms (Ats) building units shown in Figure 1(A) were generated and fed into the AL process. They were packed to dense structures, while keeping minimal distances between atoms using PACKMOL,<sup>55,56</sup> and subjected to a cook and quench procedure with temperatures up to 3000 K and pressures up to 200 GPa to find structures with high extrapolation grades. Here, for structures based on Ats and BFs, the composition was varied to cover a wider phase space, with Si and C concentrations ranging from 0 % to 100 % and the oxygen concentration from 0 to 2.2 times the Si concentration. PD building units are inspired by polymethylsilsequioxane (PMSQ), the polyorganosiloxanes RD-212, RD-684, and SILRES-604, and a fully artificial polymer made from  $\text{Si}_2\text{O}_2\text{C}$ . In the following, we will use their compositions, instead of polymer names as shown in Table 1. The AL capabilities of MTPs<sup>57</sup> and ACE potentials<sup>49</sup> were employed. We started with MTPs because the AL capabilities for ACE were implemented only recently.<sup>49</sup> Furthermore, we covered a wider variety of structures by using both codes. The training data set was considered complete when no new structures, which had a maximum density-functional theory (DFT) force of less than  $150 \text{ eV}/\text{\AA}$ , were discovered in an AL iteration. Distribution of the resulting training data with

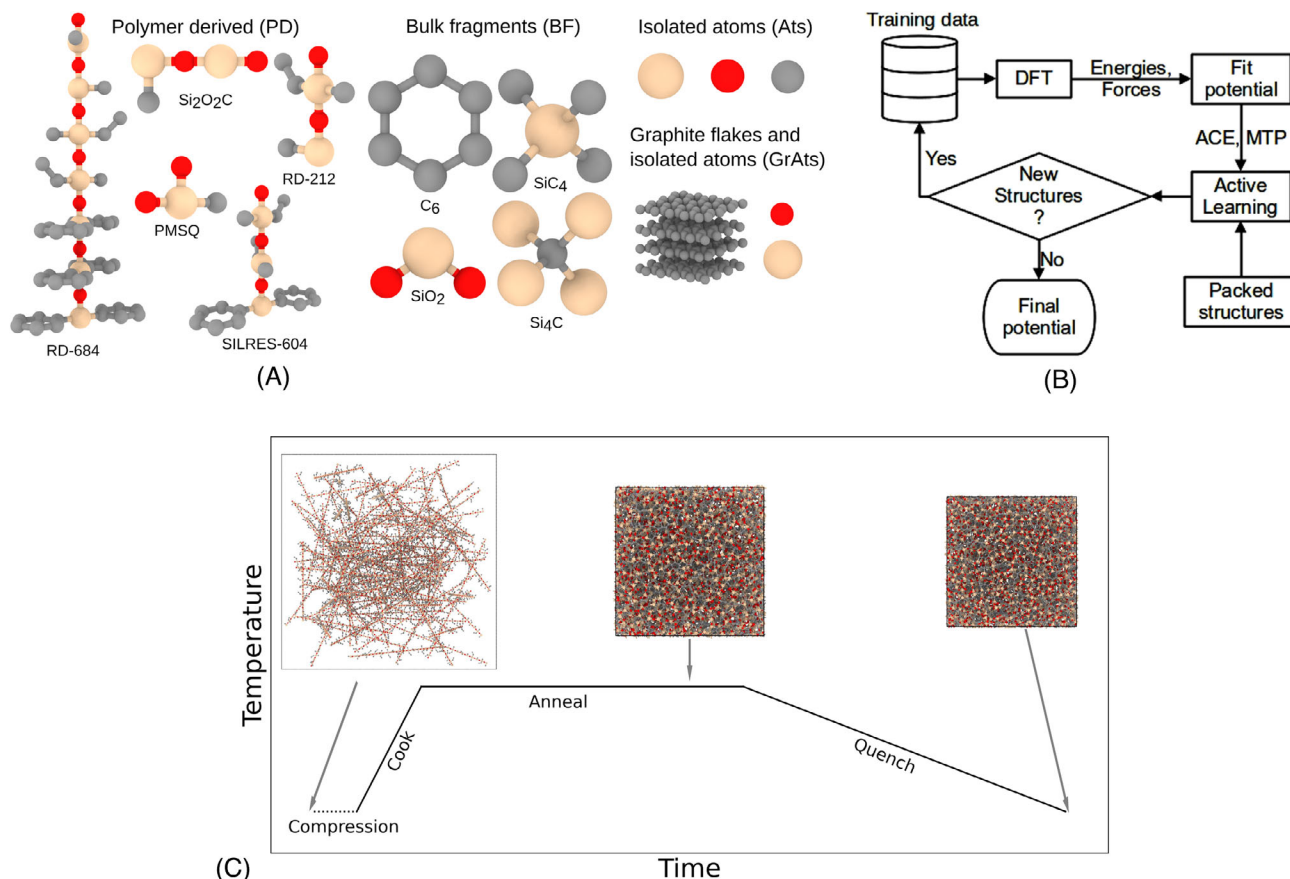


**FIGURE 1** Si-O-C structure generation and active-learning strategy. Most initial structures for the AL process were generated by densely packing smaller building blocks using the PACKMOL program. These building blocks and the nomenclature used to describe them throughout this work are shown in (A). Si is shown in beige, O in red, and C in gray. PD structures are stripped of H atoms. GrAts building blocks were used to produce large sample structures, but not in the AL process. The AL procedure employed to iteratively improve the training data is schematically shown in (B). Structures for AL and samples used in the analysis were produced using a cook and quench simulations depicted in (C). The compressions step shown as dotted line was only applied for PD and GrAts structures, where it was necessary to obtain nonporous bulk samples. For structures made from BFs or Ats, it was not necessary, because the initial packing already leads to reasonable densities.

respect to structure sizes, energies, and forces can be found in the [Supporting Information](#).

In the PD units, H atoms were stripped from the original monomers. This avoids a massive extension of the necessary training data, as the configuration space for a quaternary system is much larger than for a ternary, but keeps the polymeric backbone. This prevents a direct comparison with the experimental pyrolysis process, because the reactions taking place cannot be simulated. Due to the limits in timescale, however, this is difficult anyway. Furthermore, a dependence on the atmosphere during pyrolysis on structure formation has been observed, which would require the addition of even more elements,<sup>58</sup> which is beyond the scope of this work. We expect that the influence of missing H is smaller for higher pyrolysis temperatures, because increasing amounts of H are removed from the material in the form of gaseous products.<sup>59,60</sup> Yet, we invite researchers to extend our publicly available database<sup>61</sup> by H, to enable the simulation of pyrolysis processes.

For the test data set, the test data of the Si-O potential<sup>50</sup> were supplemented with a separately created set of Si-O-C structures. These Si-O-C test structures were created with PACKMOL at varying densities and compositions similar to the training data. Consequently, the atoms were randomly displaced.

Finally, the training and test data sets were filtered to not contain structures with a maximum force of more than  $150 \text{ eV}/\text{\AA}$ , a minimal distance between atoms smaller than  $0.6 \text{ \AA}$  or greater than  $4 \text{ \AA}$  or an energy of more than  $20 \text{ eV}/\text{atom}$  above the convex hull. Training and testing data employed in this work are publicly available (see Data availability section).

## 2.2 | Details of potentials

For the potentials, we used a cutoff of  $5 \text{ \AA}$ . The ACE and MTPs were fitted using the pacemaker<sup>40,62</sup> and MLIP

packages.<sup>48</sup> For the AL process with MTPs, a level 26 potential was employed. The intermediate ACE potentials for AL were fitted with the triple embedding  $\rho_1^{0.5} + \rho_2^1 + \rho_3^2$  and a total of 2325 basis functions. While ACE can theoretically represent MTPs,<sup>47</sup> a direct transfer of fitting coefficients is not implemented, so the potential was trained from scratch. In principle, the most straightforward way of increasing the accuracy of ACE potentials is to increase the number of basis functions. However, this considerably increases the computational cost.<sup>62</sup> Instead, we tested different embedding terms for the final potential, which is computationally very cheap. Here, we found a highly nonlinear sum of expansions  $\sum_i^n \phi_i^{\alpha_i}$  with  $n = 10$  and exponents  $\alpha_i$  0.125, 0.25, 0.375, 0.5, 0.75, 0.875, 1, 1.25, 1.5, and 2 to result in the best testing errors.

### 2.3 | Si-O-C sample structures

The structure samples used to analyze formation energies, structural features, and elastic properties contain roughly 10,000 atoms each. They were produced in a cook and quench process, as schematically shown in Figure 1(C). Here, we tested two different degrees of freedom, the influence of the composition and the effect of the precursor on the structure and properties of the final sample. The compositions of the structures correspond to the five polymeric compositions, shown in Table 1. As precursors, we employed four different types of building blocks shown in Figure 1(A). The graphite sheets in graphite flakes and isolated atoms (GrAts) structures consist of 160-atom two-layer graphite. The resulting 20 structures were used in cook and quench simulations with annealing temperatures of 1000, 1500, and 2000 K to obtain a total of 60 sample structures. Here, the annealing time was 1 ns. As shown in the Supporting Information (Section S1), this time is sufficient to reach a steady state regarding different structural features. The employed quench rate was  $1 \times 10^{12}$  K/s. PD and GrAts-based structures required an additional compression step before the cook and quench process to obtain nonporous initial structures. For this purpose, they were equilibrated at 500 K with an applied isotropic pressure of 10 GPa for 10 ps before heating them up to the annealing temperature.

### 2.4 | Simulations

DFT calculations were carried out with the same settings as used for a silica potential previously fitted<sup>44</sup> to keep the training data consistent. The plane wave code VASP<sup>63–65</sup> with projector-augmented wave<sup>66</sup> pseudopotentials and the SCAN<sup>67</sup> meta-GGA exchange-correlation were employed with a plane-wave cutoff of 900 eV and

a k-spacing of  $0.23 \text{ \AA}^{-1}$ . Classical MD simulations were carried out with LAMMPS,<sup>68</sup> applying GPU accelerated KOKKOS versions where possible. If not otherwise noted an NPT ensemble with isotropic 0 Pa pressure, Nosé-Hoover thermo- and barostats and a timestep of 1 fs were employed in the simulations.

## 3 | RESULTS

In the following, we will start by shortly presenting the results of the applied AL procedure and evaluate the newly developed MLIP. Then, we will discuss the structure of the produced Si-O-C samples based on their composition and precursors going from low to high C contents. Finally, we will relate structural features to the Young's modulus of the samples.

### 3.1 | Training and performance of the potential

The flexibility of the ACE formalism allows for an accurate description of highly complex materials, under the condition that similar atomic configurations have been part of the data used in their training procedure. In this work, an AL procedure was employed to ensure that the training data cover a large-phase space volume. Here, we started with MTPs as implemented in the MLIP package,<sup>48</sup> and continued with ACE potentials for which AL capabilities were implemented only recently.<sup>49</sup> We included structures with varying compositions and at high temperatures and pressures, as well as different defective structures that can form during MD simulations. This makes the potential applicable to a wide area of problems. Figures 2(A) and 2(B) show the resulting distribution of the training data in terms of atomic energies and volumes.

The mostly actively learned Si-O-C structures are scattered widely in this 2D representation of phase space. The pure elements and SiC structures were mostly made by hand. In combination with less compositional degrees of freedom, this leads to a comparatively narrow distribution for them. To prevent the occurrence of unphysically large forces on single atoms during MD simulations at high temperatures or pressures, we found it helpful to add SiC structures with a high density, leading to a second area with aggregated SiC structures around 4 eV/atom above the convex hull.

Energies and forces predicted using the potential agree well with those calculated using DFT over the whole range of structures. This is shown by the energy error as a function of the distance from the convex hull in Figure 2(C) and the force scatter (Figure 2D) and error plots (Figure 2E). For energies, a root mean square error (RMSE) of 24 and

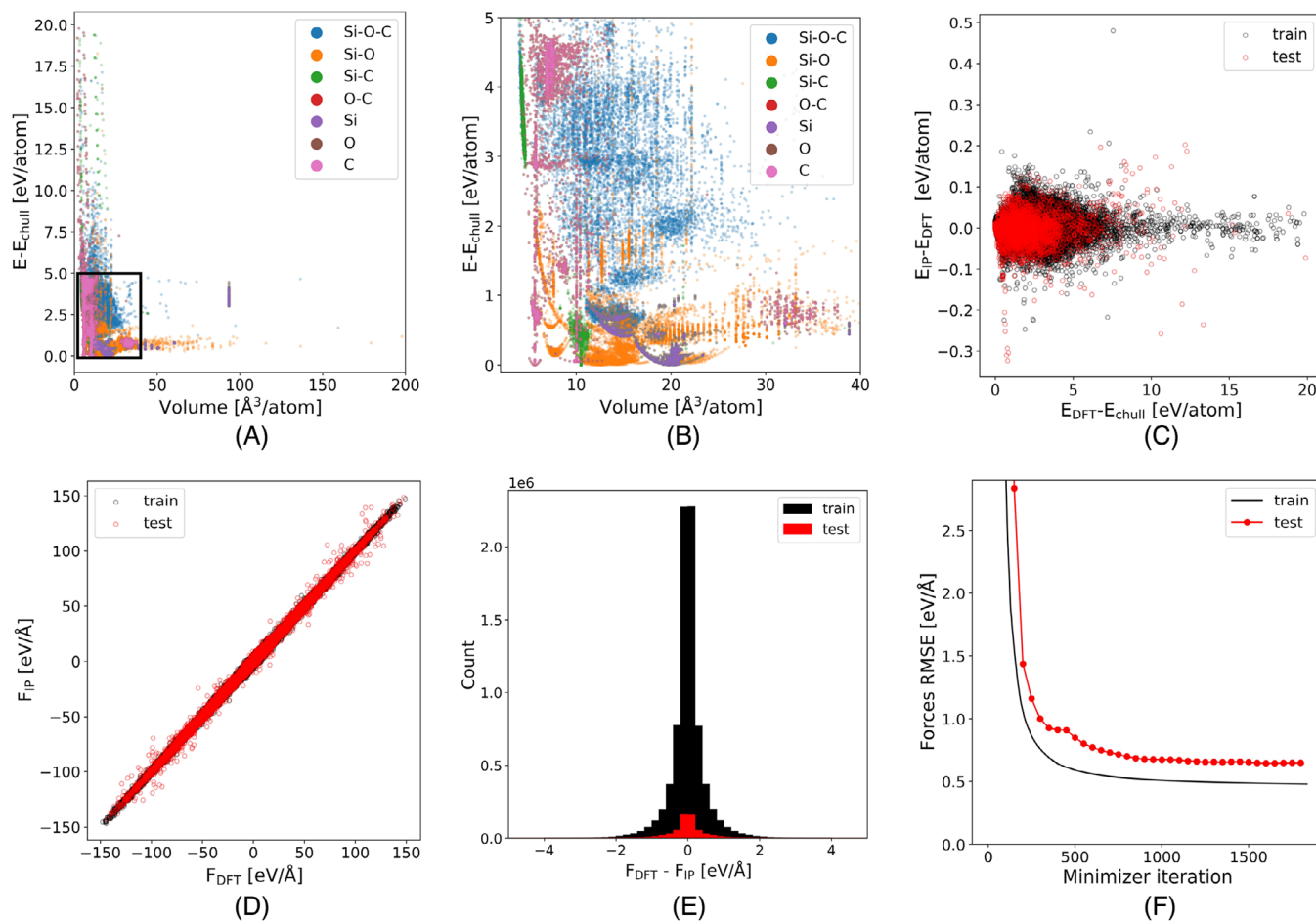


**FIGURE 2** Training data and performance of the potential. Training data resulting from the AL procedure (A) with the black box indicating the magnified region shown in (B). Error of energies as a function of the formation energy distance from the convex hull (C). Correlation (D) and histogram of force errors (E). Training and test RMSEs of forces (F) during optimization of the potential.

36 meV/atom for the training and test sets was obtained. For forces, the RMSEs were 479 and 650 meV/Å, respectively. We want to note that the higher errors for the testing set are a result from the different distribution of the structures regarding their composition and energy and not from overfitting as shown by the continuous decrease of testing error in Figure 2(F).

### 3.1.1 | Energy of sample structures

For further evaluation of the potential with respect to structures similar to those analyzed later on, the procedure described in Section 2.3 was also employed to generate one Ats sample with roughly 200 atoms for each composition listed in Table 1, respectively. This system size allows a direct comparison to DFT calculations. An annealing temperature of 3500 K was employed, to reduce the impact of the initial structural motif. The samples were fully relaxed using the ACE. Consequently, their ionic degrees of free-

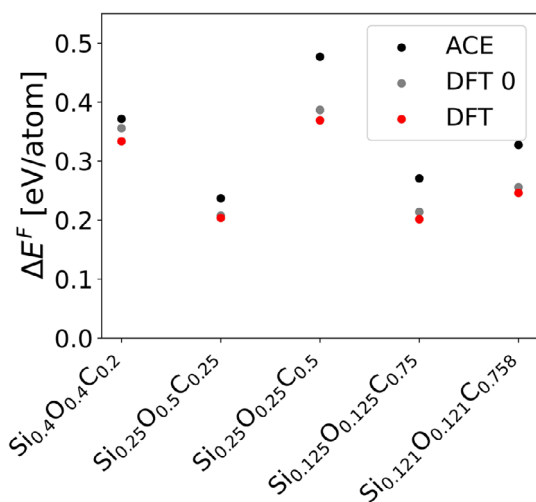
dom were relaxed using DFT. Figure 3 shows the formation energies with respect to graphite,  $\alpha$ -quartz, and  $\beta$ -SiC as calculated with the potential, with DFT without further relaxation (labeled DFT 0) and after relaxing the ionic degrees of freedom. The potential overestimates the formation energies compared to the DFT data. As shown by the relatively low-energy gain during the DFT relaxation, however, the local minima in the potential energy surface agree well between both.

### 3.1.2 | Elastic constants

In Section 3.3, elastic properties are related to structural motifs in Si-O-C samples. Here, the performance of the potential is exemplarily evaluated for the independent elastic constants of graphite,  $\alpha$ -quartz, and  $\beta$ -SiC. Table 2 lists experimentally determined and calculated values. For  $\alpha$ -quartz and  $\beta$ -SiC, excellent agreement is observed. In the case of graphite, the agreement is worse in directions

**TABLE 2** Independent elastic constants of graphite,  $\alpha$ -quartz, and  $\beta$ -SiC calculated with the ACE potential compared to experimental values.

		$C_{11}$	$C_{12}$	$C_{13}$	$C_{14}$	$C_{33}$	$C_{44}$	$C_{66}$
graphite	Exp. <sup>69,70</sup>	1060, 1109	180, 139	15, 0		36.5, 38.7	4, 5	440, 485
	ACE	1013	239	55		201	56	387
$\alpha$ -quartz	Exp. <sup>71</sup>	85–88	5–8	11–19	17–19	105–108	57–59	
	ACE	86.4	13.3	11.8	17.1	99.6	55.1	
$\beta$ -SiC	Exp. <sup>72</sup>	360–393	142–154				149–256	
	ACE	384	136				226	

**FIGURE 3** Formation energy of small Si-O-C samples. The samples were prepared similar to the large ones analyzed later on. After fully relaxing them with the ACE, their formation energy with respect to graphite,  $\alpha$ -quartz, and  $\beta$ -SiC was calculated with the potential and DFT. The latter was done as is (DFT 0), and after relaxing ionic degrees of freedom with DFT.

where Van der Waals interactions between graphite layers are important, such as  $C_{33}$ . These values are considerably overestimated. We assume that this shortcoming is caused by errors within the DFT training data, which is also not able to describe Van der Waals interactions with high accuracy. Consequently, elastic constants of graphite-rich structures could be overestimated. However, due to directional averaging and importance of other bonds within larger Si-O-C samples, we expect a small overall effect.

## 3.2 | Structure and energetics

### 3.2.1 | Si<sub>0.4</sub>O<sub>0.4</sub>C<sub>0.2</sub>

The microstructure and properties of Si-O-C compounds depend strongly on the precursor material and processing

conditions like pyrolysis temperature.<sup>7</sup> Time and length scales of the experimental processes cannot be reproduced directly in MD simulations. Instead, we used different building blocks to produce a variety of microstructures in cook and quench simulations as previously described. Examples of these initial structures are shown in the upper row of Figure 4. Exemplary samples produced via the cook and quench protocol described in Section 2.3 with an annealing temperature of 1500 K are shown in the row below. Qualitatively, the PD, BF, and Ats structures are very similar. Major differences are only found for GrAts. Here, large graphite areas are still present in the final structure. From a purely thermodynamic viewpoint, this is surprising, as one would expect that Si<sub>0.4</sub>O<sub>0.4</sub>C<sub>0.2</sub> decomposes into SiO<sub>2</sub> and SiC, but at the tested temperatures and timescales, the kinetics do not allow for such a phase separation.

To quantify differences between the structures, we calculated the Voronoi volume fractions occupied by free carbon (threefold C coordinated C) and silica phases (SiO<sub>4</sub> tetrahedra). The results are shown in Figure 5. Only the structures based on GrAts contain a meaningful amount of free carbon. As discussed previously, there is no thermodynamic driving force for the formation of graphene or graphite-like carbon, so its volume fraction is determined by the kinetics of the system and this behavior can be expected. In the GrAts structure, the volume fraction stays constant between annealing temperatures 1000 and 1500 K. At 2000 K, a slight decrease can be observed, showing that the graphite phase is kinetically stabilized up to temperatures greater than 1500 K. Regarding the silica volume fraction, a continuous increase at increasing temperatures can be observed for all structures, indicating a higher degree of phase separation. However, the data show large differences with regard to the absolute values. The largest amount is observed for the GrAts structure, followed by BFs, Ats, and finally the PD configuration. Again, this observation can be rationalized by the thermodynamics and kinetics of the system. In the GrAts structure, the unpaired Si and O atoms can quickly form

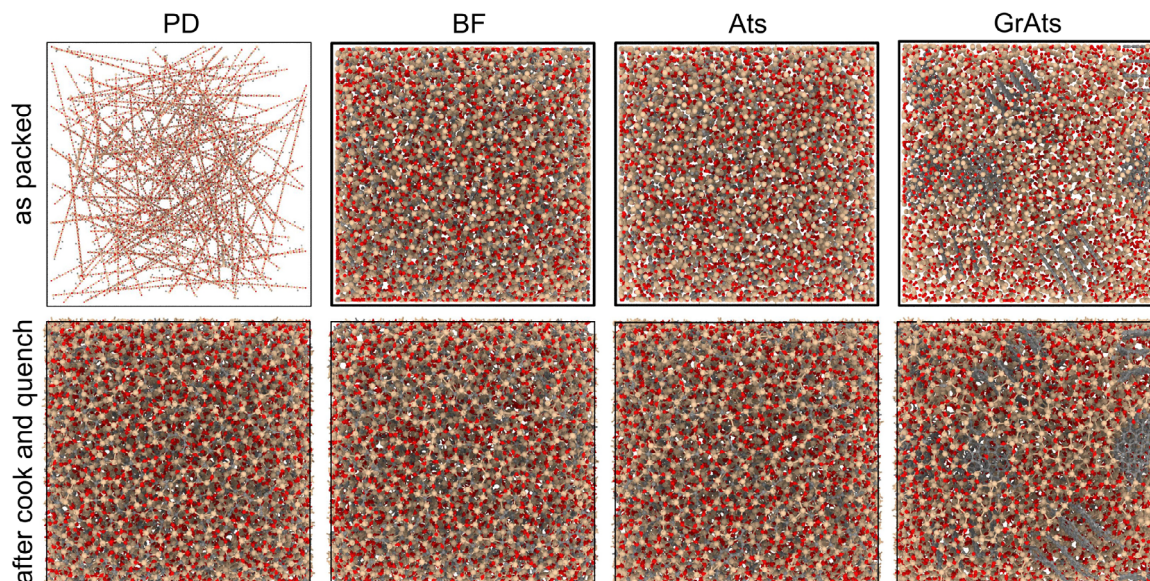


**FIGURE 4**  $\text{Si}_{0.4}\text{O}_{0.4}\text{C}_{0.2}$  assembled precursors and final structures. Shown are samples as packed with PACKMOL (upper row) and after the cook and quench process (lower row) with an annealing temperature of 1500 K for all structure prototypes. The PD, BF, and Ats structures appear to be very similar upon visual inspection. The graphite-like flakes in the GrAts-based structure are still present after processing, showing that they are kinetically stabilized, as one would expect a decomposition into  $\text{SiO}_2$  and  $\text{SiC}$  from an energetic viewpoint.

silica without interference of the carbon, because it is already bound in the graphite phase. Si-C can only form in the relatively small interface regions or requires long-range diffusion. In the BF-based structure,  $\text{SiO}_2$ ,  $\text{SiC}_4$ , and  $\text{Si}_4\text{C}$  units are already present, only requiring rotations and minor rearrangement to form the thermodynamically favored products, while the diffusion paths necessary to achieve phase separation in the atom-based structure are long and intermediate bonds can form and need to brake again. Similarly, the PD structure contains Si bonded to C and O, which needs to break before forming pure  $\text{SiO}_4$  or  $\text{SiC}_4$  tetrahedra.

The right column of Figure 5 shows the formation energy of samples with respect to  $\alpha$ -quartz,  $\beta$ -SiC, and graphite. In the case of  $\text{Si}_{0.4}\text{O}_{0.4}\text{C}_{0.2}$ , they are very close in energy, despite the significant structural differences. Especially for the structures annealed at 2000 K, the difference of nearly 0 may irritate, when considering that the system still contains a considerable amount of free carbon in the case GrAts, but this energetically unfavorable state is apparently compensated by the high fraction of very favorable silica in the system.

### 3.2.2 | $\text{Si}_{0.25}\text{O}_{0.5}\text{C}_{0.25}$

The carbon content of  $\text{Si}_{0.25}\text{O}_{0.5}\text{C}_{0.25}$  is very close to the previously discussed  $\text{Si}_{0.4}\text{O}_{0.4}\text{C}_{0.2}$ , but the different Si:O ratio leads to a different thermodynamic situation. In

equilibrium,  $\text{Si}_{0.25}\text{O}_{0.5}\text{C}_{0.25}$  should split into a pure silica and a graphite phase, whereas no SiC should form. Consequently, the formation energies of structures based on GrAts are considerably lower than those of the other precursors for  $\text{Si}_{0.25}\text{O}_{0.5}\text{C}_{0.25}$ . The difference between the Ats and GrAts structures with an annealing temperature of 1000 K is about 300 meV/atom, that is, the driving forces for phase separation are very high. Since the structures are in a steady state, this also indicates a very low mobility. For an annealing temperature of 2000 K, the difference between precursors becomes much smaller, reaching around 100 meV/atom. It is expected that the differences shrink, because the increased mobility at higher temperatures allows coming closer to the thermodynamic equilibrium. The free carbon and silica volume in  $\text{Si}_{0.25}\text{O}_{0.5}\text{C}_{0.25}$  samples increases significantly with increasing annealing temperatures. The least changes are observed for the GrAts structure, which is already close to the phase separation. Generally, the arguments regarding the kinetics of the different precursors discussed for  $\text{Si}_{0.4}\text{O}_{0.4}\text{C}_{0.2}$  also apply for  $\text{Si}_{0.25}\text{O}_{0.5}\text{C}_{0.25}$ , so similar trends can be observed, with the main differences determined by the decomposition products.

### 3.2.3 | $\text{Si}_{0.25}\text{O}_{0.25}\text{C}_{0.5}$ , $\text{Si}_{0.125}\text{O}_{0.125}\text{C}_{0.75}$ , and $\text{Si}_{0.121}\text{O}_{0.121}\text{C}_{0.758}$

$\text{Si}_{0.25}\text{O}_{0.25}\text{C}_{0.5}$ ,  $\text{Si}_{0.125}\text{O}_{0.125}\text{C}_{0.75}$ , and  $\text{Si}_{0.121}\text{O}_{0.121}\text{C}_{0.758}$  contain Si and O in a 1:1 ratio, but, in contrast to

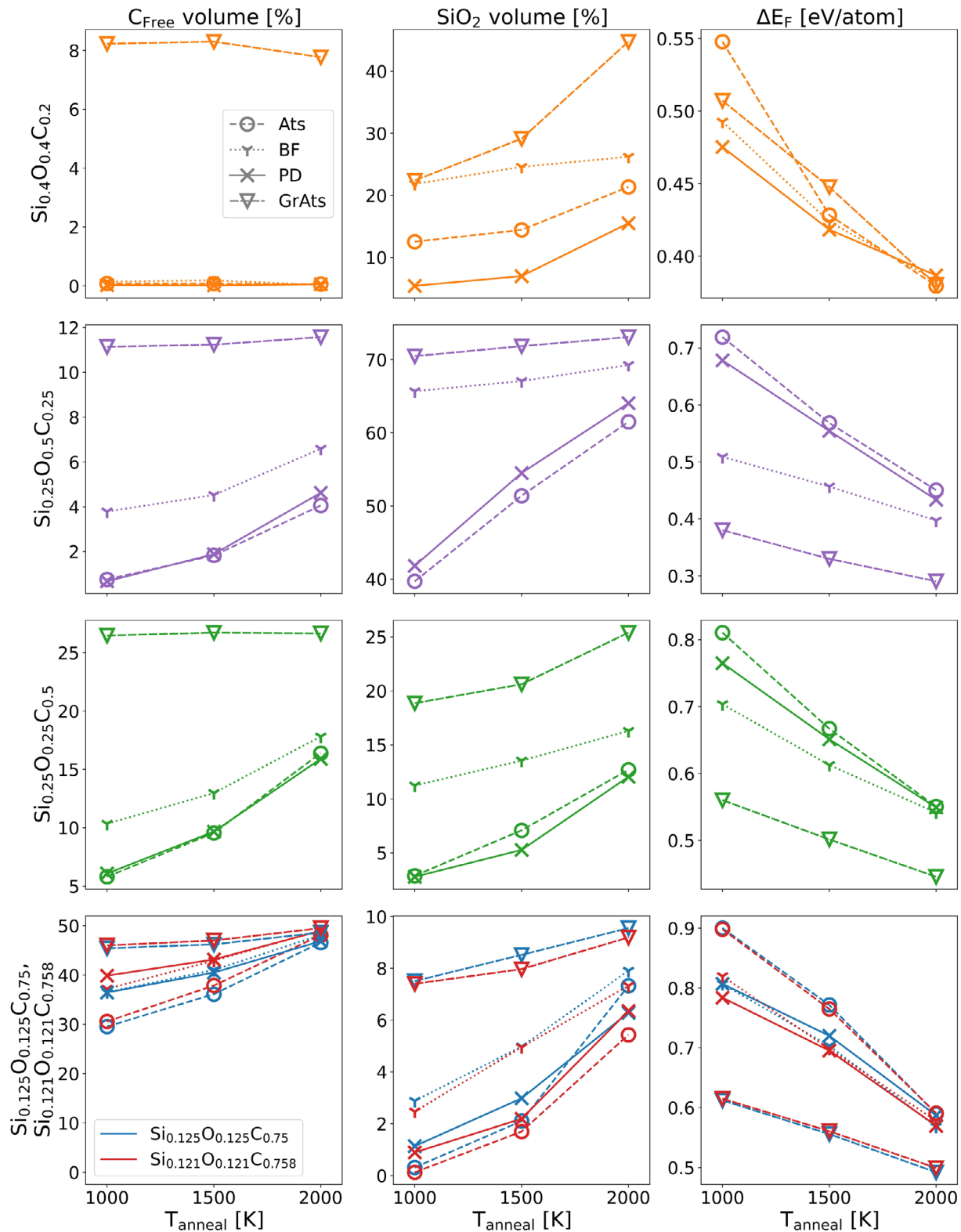


**FIGURE 5** Structure analysis and formation energies of Si-O-C samples. The left column shows the free carbon volume fraction (Voronoi volume of all threefold C coordinated C atoms), and the center column shows the silica volume fraction (Voronoi volume of  $\text{SiO}_4$  tetrahedra). The right column contains the formation energies of samples with respect to  $\alpha$ -quartz,  $\beta$ -SiC, and graphite. Rows correspond to different sample compositions.  $\text{Si}_{0.125}\text{O}_{0.125}\text{C}_{0.75}$  and  $\text{Si}_{0.121}\text{O}_{0.121}\text{C}_{0.758}$  are shown in the same row, as a direct comparison of them is interesting. Due to their compositional similarity, they allow to estimate the error between different initial random configurations. Furthermore, the PD units have a rather different initial stacking of  $\text{C}_6$  rings, but the difference in free carbon fraction is very small.



$\text{Si}_{0.4}\text{O}_{0.4}\text{C}_{0.2}$ , also excess carbon. Thus, we expect the formation of a varying amount of free carbon phase in the system and not just  $\text{SiO}_2$  and  $\text{SiC}$ . The compositional similarity of  $\text{Si}_{0.125}\text{O}_{0.125}\text{C}_{0.75}$  and  $\text{Si}_{0.121}\text{O}_{0.121}\text{C}_{0.758}$  allows us to estimate structural differences due to random placement of Ats, BF, and GrAts and the influence of different polymer-like precursors. From a comparison of structural motifs across building units and annealing temperatures, one can see that the random initialization only leads to small differences, indicating the robustness of our data. In the  $\text{Si}_{0.121}\text{O}_{0.121}\text{C}_{0.758}$  polymer,  $\text{C}_6$  rings are stacked very closely (cf. Figure 1a), which could ease the formation of graphite. However, this cannot be observed in our data. Generally, the three compounds show high free carbon contents and qualitatively similar temperature dependence for both the silica and free carbon fractions. The energetically most favorable sample is the one made from GrAts. Similar to  $\text{Si}_{0.4}\text{O}_{0.4}\text{C}_{0.2}$ , this can be explained by the high degree of phase separation, which corresponds to the thermodynamic equilibrium.  $\text{Si}_{0.125}\text{O}_{0.125}\text{C}_{0.75}$  and  $\text{Si}_{0.121}\text{O}_{0.121}\text{C}_{0.758}$  behave similar.

### 3.2.4 | Relation to model structures

As discussed previously, two models for the nanostructure of Si-O-C exist. One suggests silica-rich nanodomains, which are separated by an interconnected graphene-like carbon network.<sup>16,17</sup> The other describes the structure as graphitic inclusions in a silica-rich matrix.<sup>12</sup> The results from our simulations are shown in Figure 6. For structures that should contain graphite upon decomposition, we found the GrAts models to be energetically favorable, favoring the latter model. However, in the other samples, no graphitic carbon could be found and instead graphene-like layers spread through the system, pointing to the former. This allows us to conclude that both models are representative for two distinct stages. In early stages of structure formation, the structure is likely described by the first model, because the slow kinetics in the system prevent the formation of graphitic inclusions. With increasing temperatures and pyrolysis times, the structure evolves toward the latter model argued for by Widgeon et al., as it is lower in energy.

### 3.2.5 | Sample densities

Densities of employed samples are shown in Figure 7. The values range from 1.9 to 2.6  $\text{g}/\text{cm}^3$ , which is in line with experimental samples considered pore-free.<sup>73</sup> Samples annealed at high temperatures and compositions high

**TABLE 3** Percentage of under- and overcoordinated Si and O atoms relative to the total amount of Si and O atoms, respectively. The table exemplarily lists the values observed for Ats samples annealed at 2000 K. Additionally, values for a  $\text{SiO}_2$  Ats sample and values from Ponomarev et al.<sup>26</sup> obtained with their ReaxFF are given for comparison.

	$\text{Si}_3$	$\text{Si}_5$	$\text{O}_1$	$\text{O}_3$
$\text{Si}_{0.4}\text{O}_{0.4}\text{C}_{0.2}$	12.3	3.1	0	2.35
$\text{Si}_{0.25}\text{O}_{0.5}\text{C}_{0.25}$	0.32	1.88	6.68	0.06
$\text{Si}_{0.25}\text{O}_{0.25}\text{C}_{0.5}$	6.88	2.16	0.08	1.04
$\text{Si}_{0.125}\text{O}_{0.125}\text{C}_{0.75}$	8.88	3.04	5.12	1.6
$\text{Si}_{0.121}\text{O}_{0.121}\text{C}_{0.758}$	9.87	4.06	5.22	0.66
$\text{SiO}_2$ ACE	0.1	2	0	0.05
$\text{SiO}_2$ ReaxFF <sup>26</sup>	3.78	2.62	1.89	1.31

in carbon have lower densities.  $\text{Si}_{0.4}\text{O}_{0.4}\text{C}_{0.2}$  Ats and PD samples show an increase in density with higher annealing temperatures. We assume that this is a result of ongoing phase separation into  $\text{SiO}_2$  and  $\text{SiC}$ , without the formation of free graphite. As a result, the density lies between that of amorphous silica and  $\text{SiC}$ , with the BF sample approaching a similar value.

### 3.2.6 | Si and O coordination

A further interesting aspect of Si-O-C structures produced in MD simulations is the under- and overcoordination of atoms. Table 3 exemplarily lists percentages of wrongly coordinated Si and O in Ats samples annealed at 2000 K. Additionally, an  $\text{SiO}_2$  sample containing 3000 atoms was prepared from Ats with an annealing temperature of 3500 K, to compare it to the values given by Ponomarev et al.<sup>26</sup> for their ReaxFF. As apparent by the differences between silica and  $\text{Si}_{0.25}\text{O}_{0.5}\text{C}_{0.25}$  samples compared to the others, thermodynamically favorable network carbon is detrimental for Si coordination.

We want to note that the coordination numbers can strongly vary depending on the way they are determined. Consequently, the comparison to numbers by Ponomarev et al.<sup>26</sup> should be taken with a grain of salt. In this study, coordination numbers were obtained with fixed cutoffs per element combination using *ovito*.<sup>74</sup> Atoms were considered bonded, when their distance was less than  $0.6(R_1 + R_2)$ , where  $R$  were the Van der Waals radii  $R_{\text{Si}}$ : 2.1 Å,  $R_{\text{O}}$ : 1.52 Å, and  $R_{\text{C}}$ : 1.7 Å (default values).

Figure 8 exemplarily shows a shortcoming of this method. Here, two Si atoms are considered overcoordinated. However, it seems reasonable to assume that there is no actual bond between the Si atoms in the quantum mechanical sense, because both are already fourfold coordinated with closer atoms.

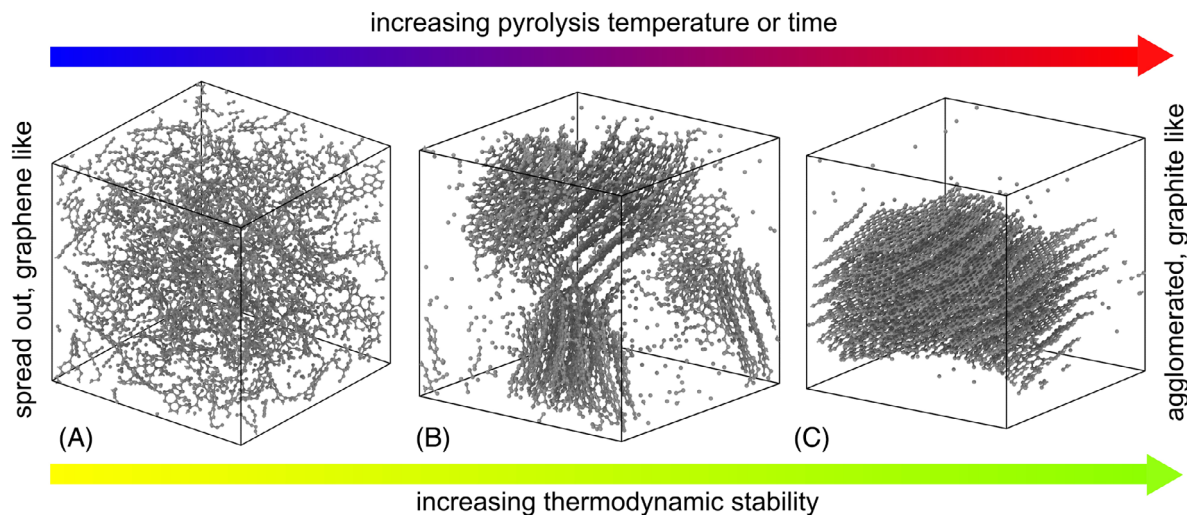


**FIGURE 6** Structure formation of free carbon phase in Si-O-C. The figures show the free carbon phase as found for  $\text{Si}_{0.25}\text{O}_{0.25}\text{C}_{0.5}$  PD sample annealed at 2000 K (A), 3000 K (B), and 3500 K (C). During annealing, an isotropic pressure of 10 GPa was applied for the latter two to prevent the formation of pores. For low pyrolysis temperatures and times, graphene-like carbon forms as argued by Scarmi et al.<sup>16</sup> and Saha et al.<sup>17</sup> based on high creep resistance. At higher temperatures energetically more favorable graphite-like agglomerates form, which are consistent with the mass fractal dimension as found by Widgeon et al.<sup>12</sup> The 3000 K looks similar to GrAts structures, showing that they can be considered as an intermediate step of structure formation.

### 3.3 | Elastic properties

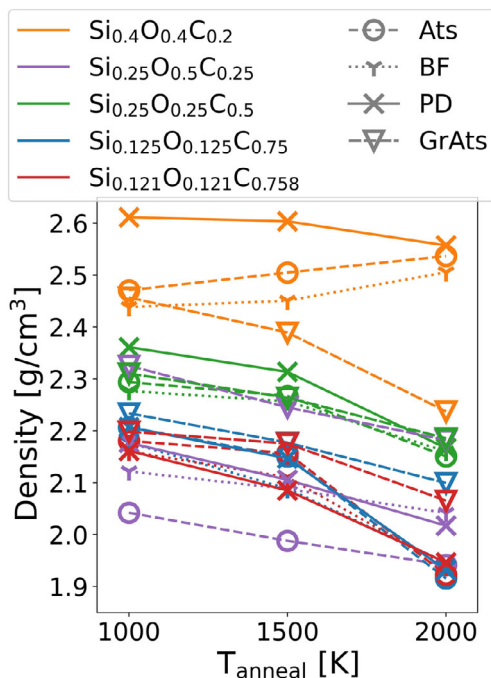
The structure of Si-O-C is highly tunable, depending on the pyrolysis conditions and precursors. An understanding of structure–property relations can therefore guide the search for processing routes that best match specific needs. Here, we investigate the structural features influencing the elastic properties of Si-O-C. For this purpose, we calculated the elastic tensors of our samples using *pymatgen*<sup>80</sup> and derived the Young's modulus

$$E = \mu(3\lambda + 2\mu)/(\lambda + \mu) \quad (1)$$

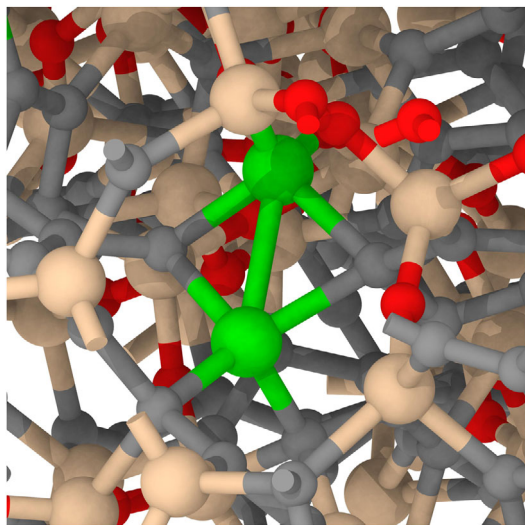
with the Lamé constants  $\mu = C_{44}$  and  $\lambda = C_{12}$ , as valid for isotropic materials. Here, the assumption of isotropy is very accurate with differences between  $C_{ij}$  that should be equivalent due to symmetry in the range of  $\pm 3\%$ . Only the GrAts structures show larger anisotropies, due to the limited amount of randomly orientated graphite flakes, leading to differences in the range of  $\pm 15\%$ . To reduce resulting errors, we averaged over the supposedly equivalent directions. The deformations applied to obtain elastic tensors are not fully reversible because the relaxation of atomic positions leads to small energy barriers on the path back to the initial state that cannot be overcome in static relaxations. Corresponding energy–strain relations can be found in the [Supporting Information](#).

Figure 9 shows the dependence of  $E$  on  $\text{SiO}_4$  volume fraction, the average amount of carbon in  $\text{SiO}_{4-x}\text{C}_x$  tetrahedra, free carbon volume fraction, and density of samples.

Generally, the modulus ranges from 70 GPa, which corresponds to  $E$  of silica glass<sup>81</sup> up to around 145 GPa. The lower bound agrees well with the experimental data, while the observed upper values are higher. However, the experimental samples contain less C overall, and a higher fraction of it is part of the free carbon phase instead of the mixed tetrahedra. The data scatter significantly between different compositions and building blocks, showing the multidimensional nature of the problem. Strong correlations of  $E$  can be seen for the  $\text{SiO}_4$  volume fraction and the amount of carbon within  $\text{SiO}_{4-x}\text{C}_x$  tetrahedra. As expected, the modulus decreases for higher silica volume fractions, approaching that of the pure amorphous phase and increases with an increasing amount of carbon in the mixed bonds. As discussed previously, GrAts-based structures contain high amounts of  $\text{SiO}_4$  tetrahedra and the C atoms are bound within the graphite inclusions, that is, they do not participate much in mixed bonding. Consequently, these structures have lower Young's moduli than structures based on other building blocks at the same compositions. Experimental studies have established empirical relations between structural features of Si-O-C and its elastic properties. Typically, it is observed that the Young's modulus increases with the amount of SiC and C within the  $\text{SiO}_{4-x}\text{C}_x$  tetrahedra and decreases with increasing free carbon volume.<sup>73,76</sup> However, as shown by Stabler et al.<sup>79</sup>, the results can differ significantly based on the kind of sample and applied measurement method. Furthermore, a recent simulation-based study by Haseen and Kroll<sup>82</sup> found a strong decrease of  $E$  with



**FIGURE 7** Sample densities. The resulting densities depend on the composition, annealing temperature, and building units. Increasing annealing temperatures lead to lower densities. Only some  $\text{Si}_{0.4}\text{O}_{0.4}\text{C}_{0.2}$  samples show a different trend, which presumably depends on the decomposition products  $\text{SiO}_2$  and  $\text{SiC}$  as discussed in the main text.



**FIGURE 8** Example of two Si atoms classified as overcoordinated (shown in green) due to definition of bonds by interatomic distance.

decreasing sample densities of equal composition employing a Tersoff-type potential. They argue that the density effect overlaps with the direct effect of the  $C_{\text{free}}$  phase, because the density of samples also strongly correlates with the amount of  $C_{\text{free}}$ . Indeed, they observed an increase

of  $E$  with higher free carbon contents for samples with same density. Similar results are observable for the ACE potential in Figure 9(D). While the overall correlation of  $E$  with the density is weak, structures with equal composition show an increase of  $E$  with higher densities. This also fits well to our observation of a weak overall correlation of  $E$  with  $C_{\text{free}}$ . If anything, when taking into account all data points, we observe a slight increase that could be related to the overestimation of some elastic constants in graphite. Considering each composition individually can also help to resolve the discrepancy with experimental results, as all of them but  $\text{Si}_{0.25}\text{O}_{0.5}\text{C}_{0.25}$  show downward trends. Therefore, we conclude that the amount of free carbon only weakly influences  $E$ , but at similar compositions, more free carbon is equivalent to lower amounts of the strong Si-C bonds, indirectly leading to a lower stiffness.

## 4 | CONCLUSION

Using multiple iterations of AL techniques implemented for MTPs and ACE potentials, we produced a highly diverse set of amorphous Si-O-C structures, spanning a large area of phase space. With the converged data set, we fitted a nonlinear ACE potential to energies and forces calculated with DFT and showed that the potential can accurately reproduce them. Due to the diversity of the training data, the potential has a large applicability range and can describe the formation of Si-O-C compounds and their properties in a large temperature and pressure range.

Applying the potential, we produced amorphous Si-O-C samples with various compositions in a cook and quench procedure. Here, we tested the influence of different initial structures on the final configuration. We found that manually added graphite agglomerates are kinetically stabilized in MD simulation times and lead to energetically favorable states compared to graphene-like sheets, if the structure contains excess C. However, their formation is kinetically hindered, and we assume that an interpenetrating network of silica-rich domains and graphene-like sheets is formed as an intermediate step during synthesis of amorphous Si-O-C.

To test and establish structure-property relations in Si-O-C, we calculated Young's moduli of the samples. We found that the silica volume fraction and the average amount of carbon in mixed  $\text{SiO}_{4-x}\text{C}_x$  tetrahedra correlate well with the stiffness across all samples. Silica reduces the stiffness and high amounts of Si-C bonds increase it. Furthermore, the free carbon volume fraction is a good indicator of  $E$  for samples with similar compositions, but not in general.

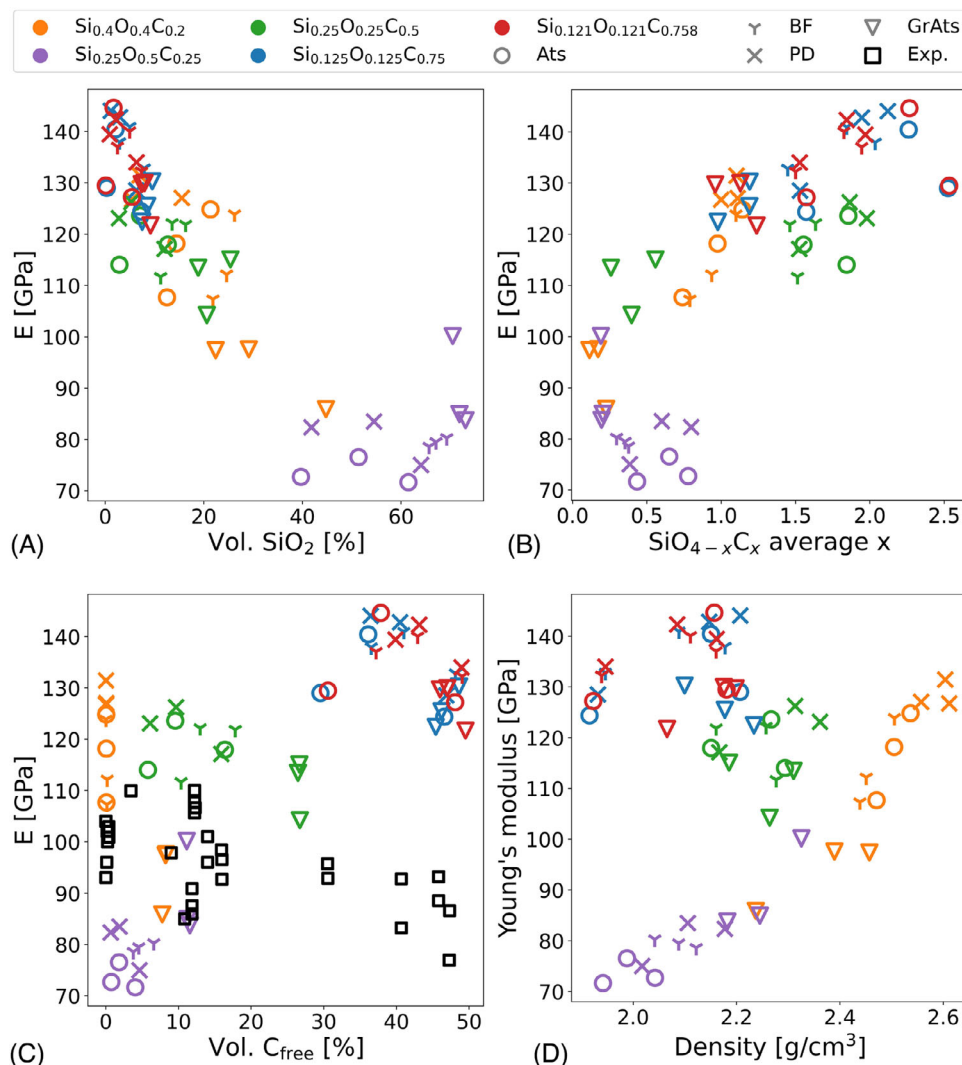


**FIGURE 9** Dependence of  $E$  on structural features. Calculated  $E$  values for samples in dependence of silica volume fraction (A), average amount of carbon in mixed tetrahedra (B), free carbon volume fraction (C), and density (D). Experimental data in (C) are taken from Refs. [3, 75–79] as collected in Ref. [79] and from Ref. [73]. Contrary to the simulated structures, the experimental data do not include samples with very high total carbon contents. Consequently, the relative frequency of SiC bonds and therefore  $E$  are lower.

We believe that the presented potential will allow detailed investigations of structure formation and properties in Si-O-C. In a broader context, we have shown that modern MLIPs can be employed to study multielement material systems that form highly complex structures. Therefore, they can greatly benefit the understanding of glassy and ceramic materials on the atomistic scale. Future works could extend the potential to describe H, enabling the reactive simulations to create Si-O-C models, or other elements of interest. The training data and potential files necessary are provided on zenodo<sup>61</sup> as part of this work.

#### ACKNOWLEDGMENTS

N. L. acknowledges Linus C. Erhard for helpful discussions. N. L. received funding from the Deutsche Forschungsgemeinschaft (DFG, German Research Foundation) under grant number 405621137 and from the


German Federal Ministry of Education and Research (BMBF) under project HeNa (FKZ 03XP0390A). J. R. acknowledges funding from the European Union's Horizon 2020 research and innovation program under Grant Agreement no. 963542. K. A. acknowledges funding by the DFG under project number 413956820. The authors gratefully acknowledge the computing time provided to them on the high-performance computer Lichtenberg at the NHR Center NHR4CES at TU Darmstadt. This is funded by the German Federal Ministry of Education and Research, and the state governments participating.

Open access funding enabled and organized by Projekt DEAL.

#### COMPETING INTERESTS

The authors declare no competing interests.

## ORCID

Niklas Leimeroth  <https://orcid.org/0009-0005-3906-4751>

Jochen Rohrer  <https://orcid.org/0000-0002-4492-3371>

Karsten Albe  <https://orcid.org/0000-0003-4669-8056>

## REFERENCES

- Li Z, Chen Z, Liu J, Fu Y, Liu C, Wang P, et al. Additive manufacturing of lightweight and high-strength polymer-derived SiOC ceramics. *Virtual Phys Prototyp*. 2020 Apr 2;15:163–77. <https://doi.org/10.1080/17452759.2019.1710919>
- Barríos E, Zhai L. A review of the evolution of the nanostructure of SiCN and SiOC polymer derived ceramics and the impact on mechanical properties. *Mol Syst Des Eng*. 2020;5:1606–41. <https://doi.org/10.1039/D0ME00123F>
- Papendorf B, Ionescu E, Kleebe HJ, Linck C, Guillon O, Nonnenmacher K, et al. High-temperature creep behavior of dense SiOC-based ceramic nanocomposites: microstructural and phase composition effects. *J Am Ceram Soc*. 2013;96:272–80. <https://doi.org/10.1111/jace.12067>
- Stabler C, Roth F, Narisawa M, Schliephake D, Heilmaier M, Lauterbach S, et al. High-temperature creep behavior of a SiOC glass ceramic free of segregated carbon. *J Eur Ceram Soc*. 2016 Nov 1;36:3747–53. <https://doi.org/10.1016/j.jeurceramsoc.2016.04.015>
- Melzi d'Eril M, Zambotti A, Graczyk-Zajac M, Ionescu E, Soraru GD, Riedel R. Effect of ultra-fast pyrolysis on polymer-derived SiOC aerogels and their application as anodes for Na-ion batteries. *Open Ceramics*. 2023 Jun 1;14:100354. <https://doi.org/10.1016/j.oceram.2023.100354>
- Vallachira Warriam Sasikumar P, Zera E, Graczyk-Zajac M, Riedel R, Soraru GD. Structural design of polymer-derived SiOC ceramic aerogels for high-rate Li ion storage applications. *J Am Ceram Soc*. 2016;99:2977–83. <https://doi.org/10.1111/jace.14323>
- Stabler C, Ionescu E, Graczyk-Zajac M, Gonzalo-Juan I, Riedel R. Silicon oxycarbide glasses and glass-ceramics: “All-Rounder” materials for advanced structural and functional applications. *J Am Ceram Soc*. 2018 Nov;101:4817–56. <https://doi.org/10.1111/jace.15932>
- Chandra C, Devina W, Cahyadi HS, Kwak SK, Kim J. Understanding lithium, sodium, and potassium storage mechanisms in silicon oxycarbide. *Biochem Eng J*. 2022 Jan 15;428:131072. <https://doi.org/10.1016/j.cej.2021.131072>
- Lu K, Erb D. Polymer derived silicon oxycarbide-based coatings. *Int Mater Rev*. 2018 Apr 3;63:139–61. <https://doi.org/10.1080/09506608.2017.1322247>
- Wen Q, Qu F, Yu Z, Graczyk-Zajac M, Xiong X, Riedel R. Si-based polymer-derived ceramics for energy conversion and storage. *J Adv Ceram*. 2022 Feb 1;11:197–246. <https://doi.org/10.1007/s40145-021-0562-2>
- Arango-Ospina M, Xie F, Gonzalo-Juan I, Riedel R, Ionescu E, Boccaccini AR. Review: silicon oxycarbide based materials for biomedical applications. *Appl Mater Today*. 2020 Mar 1;18:100482. <https://doi.org/10.1016/j.apmt.2019.100482>
- Widgeon SJ, Sen S, Mera G, Ionescu E, Riedel R, Navrotsky A. <sup>29</sup>Si and <sup>13</sup>C solid-state NMR spectroscopic study of nanometer-scale structure and mass fractal characteristics of amorphous polymer derived silicon oxycarbide ceramics. *Chem Mater*. 2010 Dec 14;22:6221–28. <https://doi.org/10.1021/cm102143z>
- Mera G, Navrotsky A, Sen S, Kleebe HJ, Riedel R. Polymer-derived SiCN and SiOC ceramics – structure and energetics at the nanoscale. *J Mater Chem A*. 2013;1:3826–36. <https://doi.org/10.1039/C2TA00727D>
- Soraru GD, D'Andrea G, Campostrini R, Babonneau F, Mariotto G. Structural characterization and high-temperature behavior of silicon oxycarbide glasses prepared from Sol-Gel precursors containing Si-H bonds. *J Am Ceram Soc*. 1995;78:379–87. <https://doi.org/10.1111/j.1151-2916.1995.tb08811.x>
- Roth F, Waleska P, Hess C, Ionescu E, Nicoloso N. UV Raman spectroscopy of segregated carbon in silicon oxycarbides. *J Ceram Soc Jpn*. 2016;124:1042–45. <https://doi.org/10.2109/jcersj2.16100>
- Scarmi A, Soraru GD, Raj R. The role of carbon in unexpected visco(an)elastic behavior of amorphous silicon oxycarbide above 1273K. *J Non Cryst Solids*. 2005 Aug;351:2238–43. <https://doi.org/10.1016/j.jnoncrystol.2005.06.008>
- Saha A, Raj R, Williamson DL. A Model for the nanodomains in polymer-derived SiCO. *J Am Ceram Soc*. 2006;89:2188–95. <https://doi.org/10.1111/j.1551-2916.2006.00920.x>
- Kroll P. Modelling and simulation of amorphous silicon oxycarbide. *J Mater Chem*. 2003;13:1657–68. <https://doi.org/10.1039/B301389H>
- Kroll P. Modeling the ‘Free Carbon’ phase in amorphous silicon oxycarbide. *J Non Cryst Solids*. 2005 May 1;351:1121–26. <https://doi.org/10.1016/j.jnoncrystol.2005.01.010>
- Kroll P. Searching insight into the atomistic structure of SiCO ceramics. *J Mater Chem*. 2010;20:10528–34. <https://doi.org/10.1039/C0JM01583K>
- van Duin ACT, Dasgupta S, Lorant F, Goddard WA. ReaxFF: a reactive force field for hydrocarbons. *J Phys Chem A*. 2001 Oct 1;105:9396–409. <https://doi.org/10.1021/jp004368u>
- Newsome DA, Sengupta D, Foroutan H, Russo MF, van Duin ACT. Oxidation of silicon carbide by O<sub>2</sub> and H<sub>2</sub>O: a ReaxFF reactive molecular dynamics study, Part I. *J Phys Chem C*. 2012 Aug 2;116:16111–21. <https://doi.org/10.1021/jp306391p>
- Soria FA, Zhang W, Duin ACT, Patrino EM. Thermal stability of organic monolayers grafted to Si (111): insights from ReaxFF reactive molecular dynamics simulations. *ACS Appl Mater Interfaces*. 2017 Sep 13;9:30969–81. <https://doi.org/10.1021/acsami.7b05444>
- Soria FA, Zhang W, Paredes-Olivera PA, van Duin Adri, CT, Patrino EM. Si/C/H ReaxFF reactive potential for silicon surfaces grafted with organic molecules. *J Phys Chem C*. 2018 Oct 18;122:23515–27. <https://doi.org/10.1021/acs.jpcc.8b07075>
- Gao H, Wang H, Zhao Z, Niu M, Su L, Wei Y. Reactive dynamics simulation study on the pyrolysis of polymer precursors to generate amorphous silicon oxycarbide structures. *J Phys Chem C*. 2018 Mar 15;122:5767–73. <https://doi.org/10.1021/acs.jpcc.7b12287>
- Ponomarev I, van Duin ACT, Kroll P. Reactive force field for simulations of the pyrolysis of polysiloxanes into silicon oxycarbide ceramics. *J Phys Chem C*. 2019 Jul 11;123:16804–12. <https://doi.org/10.1021/acs.jpcc.9b03810>
- Khaliullin RZ, Eshet H, Kühne TD, Behler J, Parrinello M. Graphite-diamond phase coexistence study employing a neural-network mapping of the ab initio potential energy surface. *Phys Rev B*. 2010 Mar 18;81:100103. <https://doi.org/10.1103/PhysRevB.81.100103>
- Deringer VL, Csányi G. Machine learning based interatomic potential for amorphous carbon. *Phys Rev B*.

- 2017 Mar 3;95:094203. <https://doi.org/10.1103/PhysRevB.95.094203>
29. Wen M, Tadmor EB. Hybrid neural network potential for multi-layer graphene. *Phys Rev B*. 2019 Nov 18;100:195419. <https://doi.org/10.1103/PhysRevB.100.195419>
30. Caro MA. Optimizing many-body atomic descriptors for enhanced computational performance of machine learning based interatomic potentials. *Phys Rev B*. 2019 Jul 30;100:024112. <https://doi.org/10.1103/PhysRevB.100.024112>
31. Rowe P, Deringer VL, Gasparotto P, Csányi G, Michaelides A. An accurate and transferable machine learning potential for carbon. *J Chem Phys*. 2020 Jul 21;153:034702. <https://doi.org/10.1063/5.0005084>
32. Shaidu Y, Küçükbenli E, Lot R, Pellegrini F, Kaxiras E, de Gironcoli S. A systematic approach to generating accurate neural network potentials: the case of carbon. *npj Comput Mater*. 2021 Apr 14;7(1):1–13. <https://doi.org/10.1038/s41524-021-00508-6>
33. Wang J, Shen H, Yang R, Xie K, Zhang C, Chen L, et al. A Deep learning interatomic potential developed for atomistic simulation of carbon materials. *Carbon*. 2022 Jan 1;186:1–8. <https://doi.org/10.1016/j.carbon.2021.09.062>
34. Qamar M, Mrovec M, Lysogorskiy Y, Bochkarev A, Drautz R. Atomic cluster expansion for quantum-accurate large-scale simulations of carbon. *J Chem Theory Comput*. 2023 Jun 22. <https://doi.org/10.1021/acs.jctc.2c01149>
35. Bartók AP, Kermode J, Bernstein N, Csányi G. Machine learning a general-purpose interatomic potential for silicon. *J Chem Theory Comput*. 2018 Dec 14;8:041048. <https://doi.org/10.1103/PhysRevX.8.041048>
36. Qian X, Peng S, Li X, Wei Y, Yang R. Thermal conductivity modeling using machine learning potentials: application to crystalline and amorphous silicon. *Mater Today Phys*. 2019 Aug 1;10:100140. <https://doi.org/10.1016/j.mtphys.2019.100140>
37. Yokoi T, Noda Y, Nakamura A, Matsunaga K. Neural-network interatomic potential for grain boundary structures and their energetics in silicon. *Phys Rev Mater*. 2020 Jan 29;4:014605. <https://doi.org/10.1103/PhysRevMaterials.4.014605>
38. George J, Hautier G, Bartók AP, Csányi G, Deringer VL. Combining phonon accuracy with high transferability in Gaussian approximation potential models. *J Chem Phys*. 2020 Jul 28;153:044104. <https://doi.org/10.1063/5.0013826>
39. Hamedani A, Byggmästar J, Djurabekova F, Alahyarizadeh G, Ghaderi R, Minuchehr A, et al. Insights into the primary radiation damage of silicon by a machine learning interatomic potential. *Mater Res Lett*. 2020 Oct 2;8:364–72. <https://doi.org/10.1080/21663831.2020.1771451>
40. Lysogorskiy Y, van der Oord C, Bochkarev A, Menon S, Rinaldi M, Hammerschmidt T, et al. Performant implementation of the atomic cluster expansion (PACE) and application to copper and silicon. *npj Comput Mater*. 2021 Dec;7:97. <https://doi.org/10.1038/s41524-021-00559-9>
41. Novikov IS, Shapeev AV. Improving accuracy of interatomic potentials: more physics or more data? A case study of silica. *Mater Today Commun*. 2019 Mar 1;18:74–80. <https://doi.org/10.1016/j.mtcomm.2018.11.008>
42. Balyakin IA, Rempel SV, Ryltsev RE, Rempel AA. Deep machine learning interatomic potential for liquid silica. *Phys Rev E*. 2020 Nov 23;102:052125. <https://doi.org/10.1103/PhysRevE.102.052125>
43. Kobayashi K, Nagai Y, Itakura M, Shiga M. Self-learning hybrid Monte Carlo method for isothermal–isobaric ensemble: application to liquid silica. *J Chem Phys*. 2021 Jul 21;155:034106. <https://doi.org/10.1063/5.0055341>
44. Erhard LC, Rohrer J, Albe K, Deringer VL. A machine-learned interatomic potential for silica and its relation to empirical models. *npj Comput Mater*. 2022 Dec;8:90. <https://doi.org/10.1038/s41524-022-00768-w>
45. Kutzhanov MK, Matveev AT, Kvashnin DG, Corthay S, Kvashnin AG, Konopatsky AS, et al. Al/SiC nanocomposites with enhanced thermomechanical properties obtained from microwave plasma-treated nanopowders. *Mater Sci Eng, A*. 2021 Sep 8;824:141817. <https://doi.org/10.1016/j.msea.2021.141817>
46. Liu Y, Wang H, Guo L, Yan Z, Zheng J, Zhou W, et al. Deep learning inter-atomic potential for irradiation damage in 3C-SiC. 2023 May 30. <https://doi.org/10.48550/arXiv.2305.19516> arXiv: 2305.19516 [cond-mat]. Available from: <http://arxiv.org/abs/2305.19516> [Accessed on: 2023 Jun 26]. Preprint
47. Drautz R. Atomic cluster expansion for accurate and transferable interatomic potentials. *Phys Rev B*. 2019 Jan 8;99:014104. <https://doi.org/10.1103/PhysRevB.99.014104>
48. Novikov IS, Gubaev K, Podryabinkin EV, Shapeev AV. The MLIP package: moment tensor potentials with MPI and active learning. *Mach Learn: Sci Technol*. 2021 Jan;2:025002. <https://doi.org/10.1088/2632-2153/abc9fe>
49. Lysogorskiy Y, Bochkarev A, Mrovec M, Drautz R. Active learning strategies for atomic cluster expansion models. *Phys Rev Mater*. 2023 Apr 12;7:043801. <https://doi.org/10.1103/PhysRevMaterials.7.043801>
50. Erhard LC, Rohrer J, Albe K, Deringer VL. Modelling atomic and nanoscale structure in the silicon–oxygen system through active machine learning. *nature communications*. 2024 Mar. *J Phys: Condens Matter*. 2024 Mar;15:1927. <https://doi.org/10.1038/s41467-024-45840-9>
51. Hjorth Larsen A, Jørgen Mortensen J, Blomqvist J, Castelli IE, Christensen R, Dułak M, et al. The atomic simulation environment—a python library for working with atoms. *J Phys: Condens Matter*. 2017 Jul 12;29:273002. <https://doi.org/10.1088/1361-648X/aa680e>
52. Jain A, Ong SP, Hautier G, Chen W, Richards WD, Dacek S, et al. Commentary: The materials project: a materials genome approach to accelerating materials innovation. *APL Materials*. 2013 Jul;1:011002. <https://doi.org/10.1063/1.4812323>
53. Rohrer J, Vrankovic D, Cupid D, Riedel R, Seifert HJ, Albe K, et al. Si- and Sn-containing SiOCN-based nanocomposites as anode materials for lithium ion batteries: synthesis, thermodynamic characterization and modeling. *Int J Mater Res*. 2017 Nov 10;108:920–32. <https://doi.org/10.3139/146.111517>
54. Šić E, Rohrer J, Ricohermoso EI, Albe K, Ionescu E, Riedel R, et al. SiCO ceramics as storage materials for alkali metals/ions: insights on structure moieties from solid-state NMR and DFT calculations. *ChemSusChem*. n/a(n/a):e202202241. <https://doi.org/10.1002/cssc.202202241>
55. Martínez JM, Martínez L. Packing optimization for automated generation of complex system’s initial configurations for molecular dynamics and docking. *J Comput Chem*. 2003;24:819–25. <https://doi.org/10.1002/jcc.10216>
56. Martínez L, Andrade R, Birgin EG, Martínez JM. PACKMOL: a package for building initial configurations for molecular

- dynamics simulations. *J Comput Chem.* 2009;30:2157–64. <https://doi.org/10.1002/jcc.21224>
57. Podryabinkin EV, Shapeev AV. Active learning of linearly parametrized interatomic potentials. *Comput Mater Sci.* 2017 Dec 1;140:171–80. <https://doi.org/10.1016/j.commatsci.2017.08.031>
  58. Wen Q, Yu Z, Riedel R. The fate and role of in situ formed carbon in polymer-derived ceramics. *Prog Mater Sci.* 2020 Apr 1;109:100623. <https://doi.org/10.1016/j.pmatsci.2019.100623>
  59. Delverdier O, Monthieux M, Mocaer D, Pailler R. Thermal behavior of polymer-derived ceramics. I. Si-C and Si-C-O systems from both commercial and new polycarbosilane (PCS) precursors. *J Eur Ceram Soc.* 1993 Jan 1;12:27–41. [https://doi.org/10.1016/0955-2219\(93\)90068-3](https://doi.org/10.1016/0955-2219(93)90068-3)
  60. Pantano CG, Singh AK, Zhang H. Silicon oxycarbide glasses. *J Sol-Gel Sci Technol.* 1999 Mar 1;14:7–25. <https://doi.org/10.1023/A:1008765829012>
  61. Leimeroth N, Rohrer J, Albe K. Potential and training data for ‘structure-property relations of silicon oxycarbides studied using a novel machine learning interatomic potential’. <https://doi.org/10.5281/zenodo.10131450>
  62. Bochkarev A, Lysogorskiy Y, Menon S, Qamar M, Mrovec M, Drautz R. Efficient parametrization of the atomic cluster expansion. *Phys Rev Mater.* 2022 Jan 24;6:013804. <https://doi.org/10.1103/PhysRevMaterials.6.013804>
  63. Kresse G, Furthmüller J, Hafner J. Theory of the crystal structures of selenium and tellurium: the effect of generalized-gradient corrections to the local-density approximation. *Phys Rev B.* 1994 Nov 1;50:13181–85. <https://doi.org/10.1103/PhysRevB.50.13181>
  64. Kresse G, Furthmüller J. Efficiency of ab-initio total energy calculations for metals and semiconductors using a plane-wave basis set. *Comput Mater Sci.* 1996 Jul 1;6:15–50. [https://doi.org/10.1016/0927-0256\(96\)00008-0](https://doi.org/10.1016/0927-0256(96)00008-0)
  65. Kresse G, Furthmüller J. Efficient iterative schemes for ab initio total-energy calculations using a plane-wave basis set. *Phys Rev B.* 1996 Oct 15;54:11169–86. <https://doi.org/10.1103/PhysRevB.54.11169>
  66. Kresse G, Joubert D. From ultrasoft pseudopotentials to the projector augmented-wave method. *Phys Rev B.* 1999 Jan 15;59:1758–75. <https://doi.org/10.1103/PhysRevB.59.1758>
  67. Sun J, Ruzsinszky A, Perdew JP. Strongly constrained and appropriately normed semilocal density functional. *Phys Rev Lett.* 2015 Jul 14;115:036402. <https://doi.org/10.1103/PhysRevLett.115.036402>
  68. Thompson AP, Aktulga HM, Berger R, Bolintineanu DS, Brown WM, Crozier PS, et al. LAMMPS - a flexible simulation tool for particle-based materials modeling at the atomic, meso, and continuum scales. *Comput Phys Commun.* 2022 Feb 1;271:108171. <https://doi.org/10.1016/j.cpc.2021.108171>
  69. Bosak A, Krisch M, Mohr M, Maultzsch J, Thomsen C. Elasticity of single-crystalline graphite: inelastic x-ray scattering study. *Phys Rev B.* 2007 Apr 30;75:153408. <https://doi.org/10.1103/PhysRevB.75.153408>
  70. Blakslee OL, Proctor DG, Seldin EJ, Spence GB, Weng T. Elastic constants of compression-annealed pyrolytic graphite. *J Appl Phys.* 1970 Jul 1;41:3373–82. <https://doi.org/10.1063/1.1659428>
  71. Pabst W, Gregorová E. Elastic properties of silica polymorphs—a review. *Ceramics-Silikaty.* 2013;57:167–84.
  72. Varshney D, Shriya S, Varshney M, Singh N, Khenata R. Elastic and thermodynamical properties of cubic (3C) silicon carbide under high pressure and high temperature. *J Theor Appl Phys.* 2015 Sep 1;9:221–49. <https://doi.org/10.1007/s40094-015-0183-7>
  73. Sorarù GD, Kundanati L, Santhosh B, Pugno N. Influence of free carbon on the Young’s modulus and hardness of polymer-derived silicon oxycarbide glasses. *J Am Ceram Soc.* 2019;102:907–13. <https://doi.org/10.1111/jace.16131>
  74. Stukowski A. Visualization and analysis of atomistic simulation data with OVITO –the Open Visualization Tool. *Model Simul Mater Sci Eng.* 2009 Dec;18:015012. <https://doi.org/10.1088/0965-0393/18/1/015012>
  75. Renlund GM, Prochazka S, Doremus RH. Silicon oxycarbide glasses: Part II. Structure and properties. *J Mater Res.* 1991 Dec 1;6:2723–34. <https://doi.org/10.1557/JMR.1991.2723>
  76. Sorarù GD, Dallapiccola E, D’Andrea G. Mechanical characterization of sol-gel-derived silicon oxycarbide glasses. *J Am Ceram Soc.* 1996;79:2074–80. <https://doi.org/10.1111/j.1151-2916.1996.tb08939.x>
  77. Walter S, Soraru GD, Bréquel H, Enzo S. Microstructural and mechanical characterization of sol gel-derived Si–O–C glasses. *J Eur Ceram Soc.* 2002 Dec 1;22:2389–400. [https://doi.org/10.1016/S0955-2219\(01\)00537-4](https://doi.org/10.1016/S0955-2219(01)00537-4)
  78. Moysan C, Riedel R, Harshe R, Rouxel T, Augereau F. Mechanical characterization of a polysiloxane-derived SiOC glass. *J Eur Ceram Soc.* 2007 Jan 1;27:397–403. <https://doi.org/10.1016/j.jeurceramsoc.2006.01.016>
  79. Stabler C, Celarie F, Rouxel T, Limbach R, Wondraczek L, Riedel R, et al. Effect of composition and high-temperature annealing on the local deformation behavior of silicon oxycarbides. *J Eur Ceram Soc.* 2019 Jul;39:2287–96. <https://doi.org/10.1016/j.jeurceramsoc.2019.02.024>
  80. Ong SP, Richards WD, Jain A, Hautier G, Kocher M, Cholia S, et al. Python materials genomics (Pymatgen): a robust, open-source python library for materials analysis. *Comput Mater Sci.* 2013 Feb 1;68:314–19. <https://doi.org/10.1016/j.commatsci.2012.10.028>
  81. Inaba S, Fujino S, Morinaga K. Young’s modulus and compositional parameters of oxide glasses. *J Am Ceram Soc.* 1999;82:3501–7. <https://doi.org/10.1111/j.1151-2916.1999.tb02272.x>
  82. Haseen S, Kroll P. analyzing the effect of composition, density, and the morphology of the “free” carbon phase on elastic moduli in silicon oxycarbide ceramics. *J Eur Ceram Soc.* 2023 Apr 1;43:1432–41. <https://doi.org/10.1016/j.jeurceramsoc.2022.11.025>

## SUPPORTING INFORMATION

Additional supporting information can be found online in the Supporting Information section at the end of this article.

**How to cite this article:** Leimeroth N, Rohrer J, Albe K. Structure–property relations of silicon oxycarbides studied using a machine learning interatomic potential. *J Am Ceram Soc.* 2024;107:6896–910. <https://doi.org/10.1111/jace.19932>